Chemical architecturation of high entropy alloys through powder metallurgy

Mathilde Laurent-Brocq, Diaa Mereib, Glwadys Garcin, Judith Monnier, Loic Perriere, Benjamin Villeroy

Laurent-Brocq, M., Mereib, D., Garcin, G., Monnier, J., Perrière, L., and Villeroy, B., Journal of Alloys and Compounds, **2020**. 835: p. 155279.
https://doi.org/10.1016/j.jallcom.2020.155279

Chemical architecturation of high entropy alloys through powder metallurgy

Mathilde Laurent-Brocq[1,*], Diaa Mereib[1], Glwadys Garcin[1], Judith Monnier[1], Loïc Perrière[1], Benjamin Villeroy[1]

[1] Université Paris-Est Créteil, CNRS, ICMPE (UMR 7182), 2 rue Henri Dunant, 94320 Thiais, France

Corresponding author

First name: Mathilde; Family name: Laurent-Brocq
E-mail: laurent-brocq@icmpe.cnrs.fr
Phone number: +33 (0)1 56 70 30 65
Postal adress : 2-8, rue Henri Dunant (bât D) F-94320 Thiais, France

Abstract

The chemically architectured alloys were proposed as a new concept of microstructure, with a multi-scale architecturation. They are composed of a solid-solution at the atomic scale, grain boundaries and composition gradients at the micronic scale and finally a 3D network of gradients at the mesoscale. Composition gradients are between two phases with the same crystalline structure but different compositions. As a first application of this concept, powders of pure Ni and CoCrFeMnNi high entropy alloy were successfully densified by Spark Plasma Sintering. Then the microstructure and mechanical properties were characterized by scanning electron microscope coupled with energy dispersive spectroscopy and electron backscattered diffraction, X-ray diffraction, nanoindentation and compression tests. The obtained chemically architectured alloys present a homogeneous distribution of the two phases with a 10 µm wide chemical gradient in between. By comparison with reference non architectured materials, the chemical architecturation induces a 35 % increase of the yield strength. Thus the concept of chemically architectured metallic alloys and composition gradients was proven as very promising: processing of this complex microstructure is possible and it induces a significant mechanical strengthening.

Keywords

Metals and alloys; powder metallurgy; mechanical properties; scanning electron microscopy, SEM; X-ray diffraction

1. Introduction

Metallic alloys are essential for many industrial applications, as energy production, aeronautics, automotive sectors or building. During the past decades, the mechanical properties of existing alloy families, such as steels or super-alloys, have been largely improved through the control of the microstructure and some chemical adjustments. More precisely, the well-known strengthening strategies of precipitation, dilute solid solution or strain hardening have been successfully applied. Nevertheless, those approaches seem to have reached their limit while there is still a need of a significant improvement of the properties. Indeed, some large holes exist in Ashby's maps of properties [1], especially on the mechanical strength-ductility map. For most of the metallic alloy families, mechanical strength and ductility are mutually exclusive. This is often referred to as the strength-ductility trade-off [2] and this can be explained by two main reasons. First, in most conventional strengthening strategies, some very hard but fragile phases and/or some weakening interfaces (i.e. around which stress is highly localized) are formed. Second, according to the Consider criterion, if the work-hardening is constant, increasing the yield strength will automatically lead to the decrease of the ductility [1]. This phenomenon is even emphasized by the decrease of work-hardening which is often induced by strengthening elements, for example when decreasing the grain size [3].

To overcome the strength-ductility trade-off, new families of alloys, like dual-phase steels [4, 5], TWIP and TRIP steels [6] or harmonic structures [7], which are based on new strengthening strategies, are emerging. In line with this ongoing effort, we propose here composition fluctuations as a new possible strengthening mechanism, which preserves ductility. This idea is inspired from the early stages of spinodal decomposition, in which chemical gradients are also present, at a nanometric scale, between the two phases in formation. Spinodal microstructure are formed by casting and annealing. They can induce an increase of the yield strength, which was proposed to be due to a coherency strain related mechanism [8, 9]. Spinodal decomposition also exhibits several drawbacks. First, the increase of yield strength is very sensitive to the processing conditions [10, 11] and thus is difficult to control [12]. Moreover, the spinodal decomposition, which is related to the thermodynamic properties [13], exists for specific and limited compositions, which restricts, among other things, the possibility to tune the lattice misfit and thus the strain coherency. Finally, spinodal microstructure can induce embrittlement and is sometimes studied in order to avoid it, as in Fe-Cr alloys [11, 14].

To avoid these drawbacks, composition fluctuations will be included in a new microstructure, for which we propose the name "chemically architectured metallic alloys" (Fig. 1). The idea is to create a continuous variation between two compositions (i.e.: *A* and *B*) having the same crystallographic structure (Fig. 1c). By appropriately choosing compositions *A* and *B*, the lattice parameter will significantly vary with composition, which will induce local coherency strains. Thus, as in early stage spinodal microstructure, these chemical gradients are expected to be strengthening. At the mesoscale, the gradients will form a 3D network and they will be surrounded by domains of composition *A* and *B* with size of tens of microns (Fig. 1d). These characteristic lengths, which are intendedly larger than in spinodal microstructure, should allow dislocations pile-up and

multiplication, which is in favor of work-hardening and thus of a preserved ductility [7]. Each domain of *A* and *B* will contain grain boundaries (Fig. 1b).

Powder metallurgy is chosen for processing of chemically architectured alloys because of its tunability. This is another difference with spinodal microstructures, which usually rely on bulk casting and thermomechanical treatments. Powders of *A* and *B* need to be sintered with a double objective: (i) to densify the powders into a bulk material, (ii) to create chemical gradients by species diffusion at the interface of *A* and *B* powder grains. Spark Plasma Sintering (SPS) was chosen for its capacity of fast heating and cooling [15-17], which should favor the control of the gradient width.

The goal of this study is to provide an experimental proof of concept for this new family of materials, the chemically architectured metallic alloys. More specifically, the objective is to demonstrate for one model alloy the feasibility of processing and the improvement of the mechanical properties which is induced. High entropy alloys (HEA) have been selected as good candidates. HEA is a relatively new family of metallic alloys [18], which are multi-components and in which all components are very concentrated [19]. Some compositions, like the equimolar CoCrFeMnNi HEA [20, 21], are single-phase (i.e.: a unique multi-component face centered cubic solid solution). This solid-solution adds another scale to the architectured microstructure (Fig. 1a). Moreover, the Co-Cr-Fe-Mn-Ni system exhibits a very wide composition range of stability of the solid solution [22], which is favorable to form the aimed chemical gradients. The equimolar CoCrFeMnNi and pure Ni were selected as compositions *A* and *B* because, on the CoCrFeMn-Ni isopleth, the fcc solid solution domain ranges from pure Ni to CoCrFeMnNi for a large domain of temperature [22, 23] and the lattice misfit between them is one of the most significant within this system [24, 25].

In this paper, after choosing appropriate processing conditions, the microstructure of the obtained materials was characterized, the mechanical properties were measured macroscopically by compression tests and locally by nanoindentation. Finally, the unprecedented aspects of processing and characterization were discussed and the strengthening contributions of each element of the microstructure were analyzed.

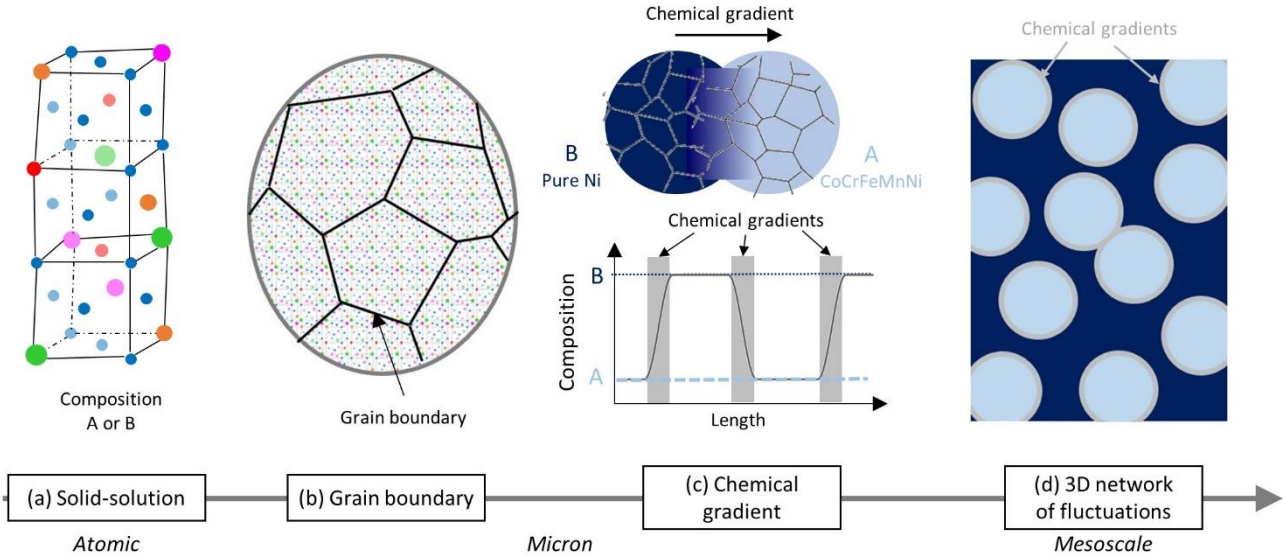

Fig. 1 : Scheme of the concept of chemically architectured metallic alloys. The microstructure is represented at various length scales.

2. Materials and methods

The equimolar CoCrFeMnNi powder was produced by gas atomization thanks to the commercial process of Nanoval GmbH & Co. In a previous study, it was shown that ball-milling is not an efficient technique to produce HEA powders because, among other things, the shape and granulometry of powder grains are not controlled [26]. Thus gas atomization, which has already been successfully used to produce spherical and micronic CoCrFeMnNi powders [27], was preferred. To decrease the content of manganese oxides, the powder was efficiently treated in a hydrochloric acid solution. The content of C, as measured by combustion infrared absorption, was as low as 0.005 at.%. A high purity (> 99.996 wt. %) commercial Ni powder was used. For the sake of simplicity, it was chosen to have equal fraction and width of domains for CoCrFeMnNi and Ni. Thus both powders were sieved to have a powder grain size ranging from 20 to 36 µm. For the architectured samples, CoCrFeMnNi and Ni sieved powders were mixed with a 1:1 mass ratio during 30 minutes in a Turbula® mixer (WAB Group, Switzerland).

The sintering equipment was the Fuji 515S Spark Plasma Sintering (SPS) equipment of the "Plateforme Ile-de-France de Frittage". Graphite mold lined with graphite paper with a diameter of 10 mm was used. Around 2 g of powder was sintered, which results in pellets with an approximate thickness of 3 mm. Sintering was performed under vacuum. The temperature was increased up to a maximum temperature T_{max} of 850°C with a heating speed of 100°C.min^{-1}. Once T_{max} was reached, an uniaxial pressure of 100 MPa was applied to the pellet. The maximum temperature was maintained for a total duration of either 5 or 15 min. Afterwards, load and temperature were decreased in a few minutes. The 1:1 mixtures of CoCrFeMnNi and Ni powders were sintered as well as the CoCrFeMnNi and the Ni powders alone for reference. For the pellet of pure Ni powder the sintering conditions were modified in order to get a similar porosity compared to other pellets. A pressure of 200 MPa was applied at the beginning of heating, and a duration of the plateau of 15 min was chosen. The other sintering parameters were unchanged.

The samples are named *Y-X* where (i) *Y* indicates the present phases and can be (HEA+Ni) for chemically architectured alloys, HEA or Ni for single-phase reference samples; and (ii) *X* is the state

of the samples and can be P for powder or S for sintered pellets. Sintered samples are labelled either 1 or 2 for a plateau duration of 5 or 15 min respectively. They are listed in Table 1.

The sintered pellets was mechanically polished to remove the surface layers which may contain undesired carbides. Indeed, it was already shown that CoCrFeMnNi is sensitive to carbon contamination from the graphite mold and paper during SPS [26]. The density of the pellet was measured using the buoyancy technique which utilizes Archimedes' principle. Samples, including the mixture of gas atomized CoCrFeMnNi and Ni powders, were characterized by X-Ray Diffraction (XRD) on a PANAlytical X'Pert Pro diffractometer using the Co-K_α radiation at a wavelength of 0.178897 nm. Pattern matching was performed on all X-ray diffractograms, using the FullProf Software. It permits to determine the lattice parameters [28]. Microstructural characterization was performed using a Zeiss Merlin Field Emission Scanning Electron Microscope (FE-SEM) coupled with an Energy Dispersive X-ray Spectrometer (EDS) and an Electron BackScattered Diffraction detector (EBSD) from Oxford Instruments. Both detectors are driven by AZtec operating system.

To calculate the average chemical composition after SPS sintering, for the single-phase HEA-S1 and HEA-S2 samples, the average chemical composition was measured by EDS on two areas of around 900×700 µm². For architectured (HEA+Ni)-S1 and (HEA+Ni)-S2 samples, 10 EDS spectra point analyses were collected in the middle of each phase and for each sample. The reported values are the average. For (HEA+Ni)-S1 and (HEA+Ni)-S2, five EDS profiles per samples were also collected along lines which are perpendicular to HEA/Ni interfaces. The electron energy was 15 keV, the step size was 150 nm and the length of the line is around 30 µm. These profiles were used to calculate the width of the chemical gradient for each element with the following procedure (Fig. S1). The difference Δ between the maximum $[C]_{max}$ and minimum $[C]_{min}$ of the concentration of element *C* was calculated. Then the points with a concentration equal to $[C]_{max} - 0.05 \times \Delta$ and $[C]_{min} + 0.05 \times \Delta$ were determined. The chemical gradient width is defined as the difference between the abscissa of these two points.

For architectured samples, areas with a dimension of 230×170 µm² were mapped by EBSD coupled with EDS, with a step size of 300 nm and an electron energy of 20 keV. This coupling permits to distinguish the HEA and Ni phases based on their difference of composition. This would not have been possible by a standard EBSD characterization because the HEA and Ni phases have the same crystallographic structure with too close lattice parameters. The grain size was determined by applying the circular intercept method [29] on band contrast EBSD images. Single-phased samples were also characterized by standard EBSD. Their grain size was determined by averaging the diameter of the detected grain on EBSD mapping. For all samples, Σ3 boundaries were not taken into account.

Next, the mechanical properties were measured by uniaxial compression tests at room temperature. Samples were cut into parallelepiped with a height of 4 mm and a section of 2.5×2.5 mm², giving an aspect ratio of 1.5. The compression faces of the samples were grounded perfectly parallel by mechanical polishing to ensure stress uniaxiality. For each composition and sintering conditions, two samples were tested. An Instron 5966 machine with a maximum force of 10 kN was used. Samples were compressed at a constant ram speed that provided an initial strain rate of 0.001 s^{-1}. When a force of 6000 N was reached, the test was interrupted. The linear compliance of the machine was experimentally determined to be of 0.026 $m.N^{-1}$ in the force range

of 0 to 6000 N. Strains were accordingly corrected. The yield strength was determined at 0.2 % of plastic strain.

Finally, the local mechanical properties were characterized by nanoindentation using a TI950 Hysitron indenter, which was equipped with a Berkovich diamond tip. The quality of the surface was checked on surfaces of 10×10 µm² by Scanning Probe Microscopy (SPM) [30], which consists in scanning the sample surface with the nanoindenter tip. It is underlined that the polishing procedure has topographically revealed the two phases in chemically architectured samples. Consequently, it was possible to optically distinguish both phases within the nanoindenter. Despite the significant slope at the interface of both phases, the surface angle in the middle of HEA or Ni domains, as locally measured by SPM, was smaller than 1°, which does not influence nanohardness measurements [30]. For chemically architectured samples (i.e.: (HEA+Ni)-S1 and (HEA+Ni)-S2), a minimum of 15 indents were selectively positioned in the middle of HEA and Ni phase respectively. For the single-phase samples (i.e.: HEA-S1, HEA-S2 and Ni-S2), 15 indents were randomly placed on the whole samples. Each indentation was performed with a constant strain rate loading of $\dot{h}/_h = 0.05\ s^{-1}$, where *h* is the indentation depth. The load was increased up to 12 mN, maintained during 5 s and unloaded for 5 s at a constant loading rate. The maximum indent depth was around 400 nm, depending on the composition. The continuous stiffness measurement (CSM) was set up at a frequency of 200 Hz, with an amplitude between 1 and 2 nm. CSM was used to calculate reduced elastic modulus E_r and hardness *H* versus indentation depth *h* by the Oliver and Pharr method (Fig. 7a). E_r and *H* were averaged for indentation depth between 350 and 400 nm (as indicated by the black arrow on Fig. 7a). They were also averaged on the 15 indents performed on each sample and within each phase. The averaged values are named $\overline{\boldsymbol{E}}$ and $\overline{\boldsymbol{H}}$**.** The given uncertainty corresponds to the standard deviation on the averaged values. The reduced elastic modulus E_r has to be converted into the Young modulus *E* [31]. Poisson's ratio of 0.304 and 0.265, which were measured on pure Ni and CoCrFeMnNi HEA [32], were used for Ni and HEA phases respectively.

3. Results

3.1. Processing

At first the morphology of the HEA (CoCrFeMnNi) and pure Ni sieved powders, which were named HEA-P and Ni-P, were characterized by SEM (Fig. 2). HEA-P (Fig. 2a) is a spherical powder with a dendritic segregation which can be observed on the surface of the grains. It is mentioned that as-cast bulk HEA exhibit similar dendritic microstructure [21]. The powder grain size ranges from 20 to 36 µm as aimed by the sieving procedure. The powder grains of Ni-P (Fig. 2b) is round, with a significant surface roughness. They are less regular than HEA powder. Moreover, the powder grains are significantly smaller than 20 µm, despite sieving. This may be due to a weak coherency of the powder grains, which can fracture after sieving. However, it does not compromise the homogeneous distribution of the two phases in the sintered samples as will be seen later. The HEA-P, Ni-P and the mixture of both powders (HEA+Ni)-P were characterized by XRD (Fig. 5a). It was checked that they are composed of a face-centered cubic (fcc) phase with a lattice parameter of 0,35938 (1) nm for CoCrFeMnNi and 0,35238 (1) nm for pure Ni either in the single-phase samples

HEA-P and Ni-P or in the mixture (HEA+Ni)-P (Table 1). This is in quantitative agreement with previous results on bulk CoCrFeMnNi [24] and Ni [33].

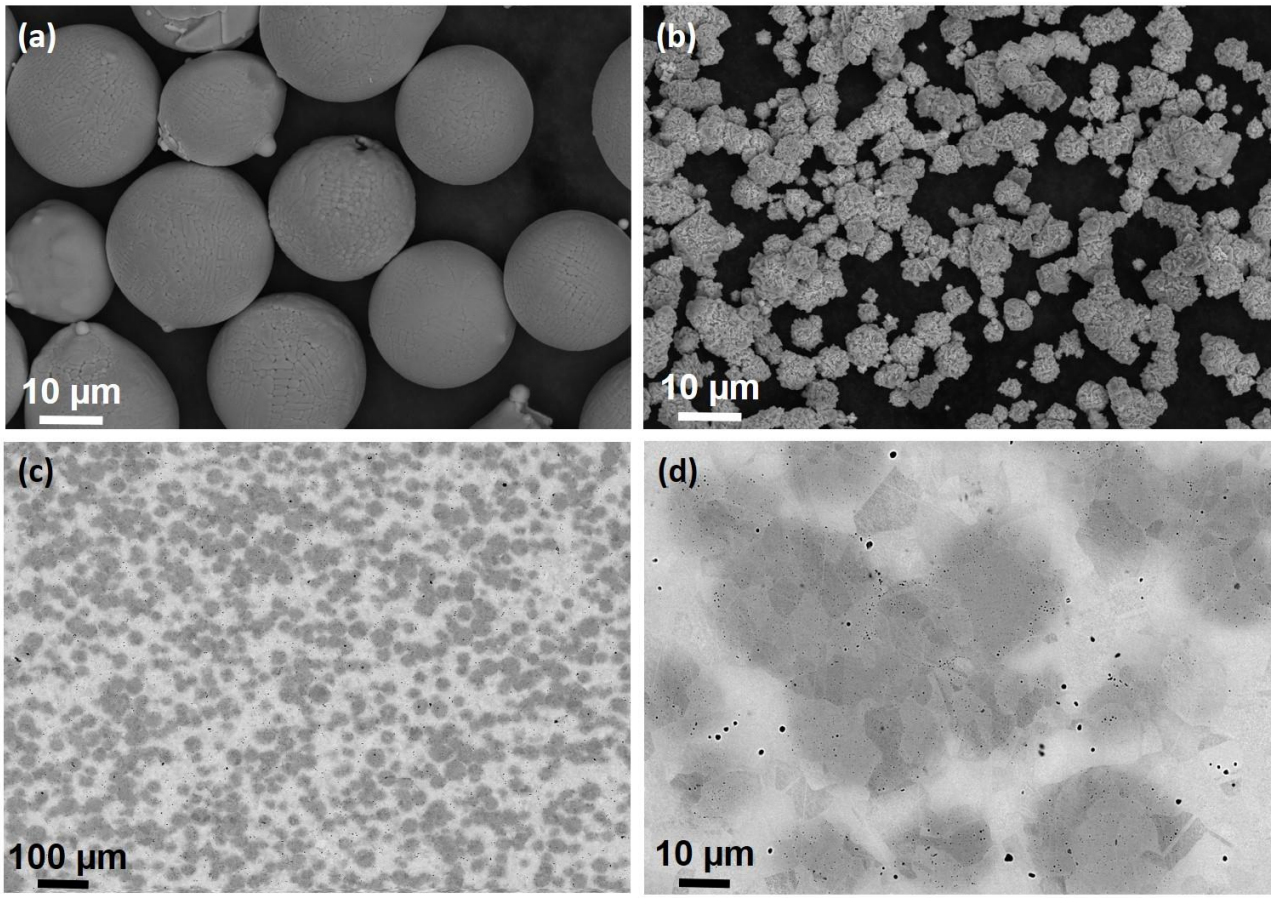

Fig. 2 : Scanning electron microscope images in backscattered electron mode (BSE) of the starting powders HEA-P (a) and Ni-P (b); and of a chemically architectured metallic alloy (HEA+Ni)-S1 at two different magnifications (c and d).

For sintering, the same maximum temperature and pressure (i.e: 850°C and 100 MPa) which were previously used for milled powders of a HEA [26] were chosen. The maximum temperature was maintained for a total duration of either 5 (condition 1) or 15 (condition 2) minutes, in order to test the effect on the growth of the chemical gradients. These conditions were applied to the 1:1 mass ratio mixture of HEA and Ni powders to create chemically architectured alloys and to the HEA powders only, to have a reference alloy (i.e. without chemical gradients). To fully densify the Ni powder only, a higher pressure of 200 MPa was needed. Table 1 shows the measured volume fraction of porosity of (HEA+Ni)-S1, (HEA+Ni)-S2, HEA-S1, HEA-S2 and Ni-S2. The low values (< 1%) indicate that the chosen SPS conditions allow to reach a full sintering not only for HEA atomized powders, as already achieved in [26], but also for the HEA and Ni mixture of powders. This fully dense aspect is confirmed by SEM images (Fig. 2c and d): there is no porosity spotted on the surface of the sample. More specifically, it can be noticed that, at the same sintering conditions, the volume fraction of porosity of HEA-S is slightly smaller than (HEA+Ni)-S. For example, it reaches a value of 0.14 and 0.74 % for HEA-S2 and (HEA+Ni)-S2 respectively. It is very likely due to the addition of Ni which has a higher melting temperature (1455°C) compared to CoCrFeMnNi HEA (1340°C [21, 34]) and is thus more difficult to sinter as was experienced for Ni-S2. The increase of the plateau duration

also improves the densification. Indeed, the volume fraction of porosity of samples sintered during 15 minutes is lower than the one of samples sintered during 5 minutes.

3.2. Microstructure characterization

A longitudinal section of (HEA+Ni)-S1 was characterized by SEM in backscattered electron mode (BSE) (Fig. 2c and d). On Fig. 2c, a homogeneous distribution of round particles (dark grey) in a percolating matrix (light grey) is observed. However, the higher magnification image (Fig. 2d) shows a local agglomeration of the round particles. Some black dots, with an approximate size of 500 nm, can be observed in the two phases. They have been identified as oxides enriched in Cr and Mn by EDS point measurements.

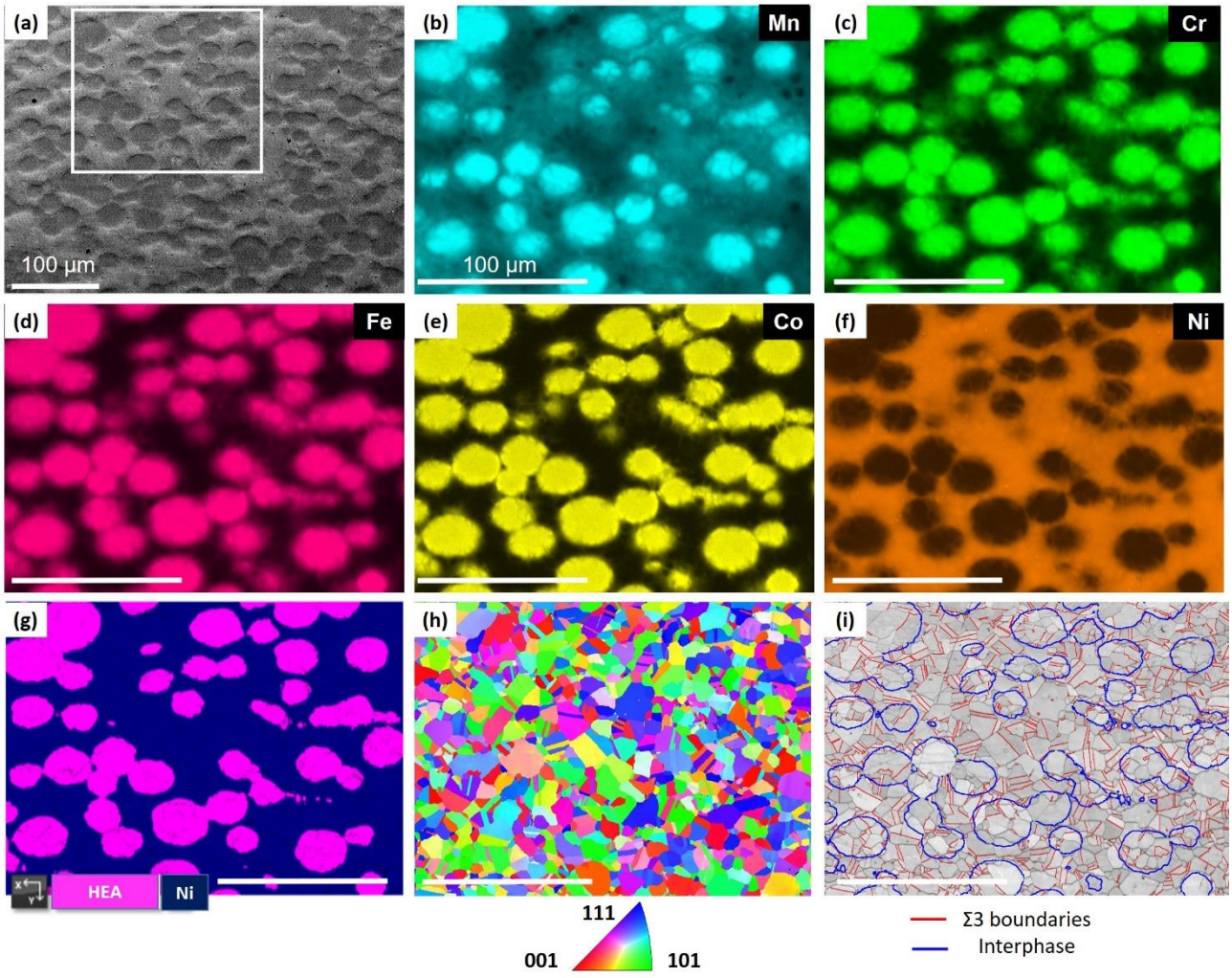

Fig. 3 : Energy Dispersive X-ray Spectrometer (EDS) coupled with Electron BackScattered Diffraction (EBSD) mapping of the chemically architectured alloy (HEA+Ni)-S1 (a) Scanning electron microscope image in backscattered electron mode (BSE). The white square indicates the area of EDS and EBSD mapping. (b, c, d, e and f) EDS mapping of Mn, Cr, Fe, Co and Ni respectively. (g) HEA and Ni phases repartition map (h) Orientation map with the corresponding standard stereographic triangle (right down corner), (i) Band contrast image on which Σ3 boundaries and the interphase (i.e.: the limit between HEA and Ni phases) are indicated. The scale is the same for (b) to (i).

Afterwards, EDS maps (Fig. 3b-f) permit to identify that the percolating matrix is the Ni phase and that the round particles are the HEA phase. The blurred interfaces between the two phases are a first indication of the presence of the chemical gradients. It can also be noticed that the Mn diffusion

is most significant than the one of the other elements (Fig. 3b). Actually, Mn is present nearly everywhere within the Ni phase. Indeed, the average composition measured in the middle of Ni domains indicates a content of around 6 at. % of Mn (Table 1). This phase is now a diluted solid solution of Mn in Ni. The average composition of the HEA phase remains equimolar (Table 1). It has to be underlined that this is only the case in the middle of the domains. This will be illustrated later on.

Next, in order to evaluate the width of the chemical gradient as well as its evolution as a function of the heating duration, line profiles were performed by SEM-EDS analysis for (HEA+Ni)-S1 and (HEA+Ni)-S2. Fig. 4b shows an example of such a line profile measured through a HEA domain for (HEA+Ni)-S2. The corresponding SEM-BSE image is depicted on Fig. 4a. When starting from the left, in the Ni phase (light grey on SEM image), the content of Ni gradually decreases while the content of Co, Cr, Fe and Mn increases. This area of composition variation is the desired chemical gradient. The content of each element reaches 20 at. %, which corresponds to the equimolar HEA (dark grey on the SEM image). Afterwards, the content of Ni increases again while the content of the other ones decreases and then stabilizes. The composition evolution of Co, Cr and Fe is very similar (i.e.: their curves overlap). The evolution of Mn is different. Indeed, it varies with a smaller slope and never reaches 0 at. % in the Ni phase, contrary to Co, Cr and Fe. This is in agreement with the average composition of the Ni phase (Table 1). In the HEA phase, the composition is equimolar in the middle of the phase, as reported in Table 1. However, anywhere else, there is a Mn depletion, which is more or less important, depending on the distance from the interface. A line profile of another gradient is depicted in Fig. S2 and exhibits the same tendency. The calculated averages width for each element and each sample is reported in Fig. 4c and Table 1. It is approximately of 10 µm and is similar for all elements. Indeed, considering the standard deviation, the gradient width for Mn does not appear significantly larger than for the other elements. Moreover, the average gradient size of (HEA+Ni)-S1, (HEA+Ni)-S2 exhibits no significant difference. Thus, surprisingly, increasing the heating duration from 5 to 15 minutes has not enhanced the gradient growth.

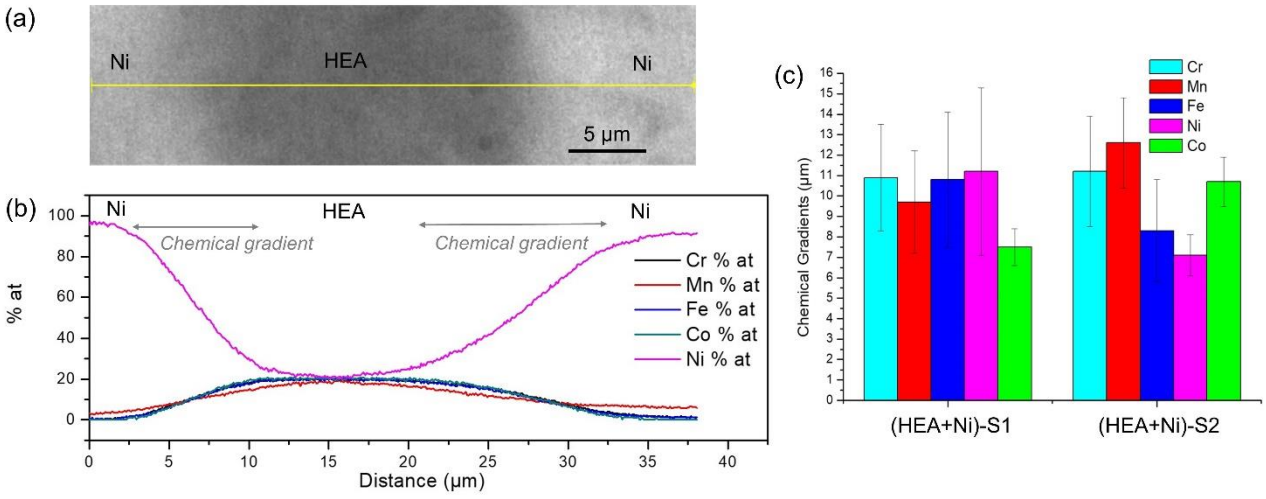

Fig. 4: Measurements of chemical gradient width in chemically architectured alloys by Energy Dispersive X-ray Spectrometer (EDS) line profile. (a) Scanning electron microscope image of (HEA+Ni)-S2. The yellow line localizes the EDS profile which is plotted in (b). (c) Average chemical gradient widths of Cr, Mn, Fe, Ni and Co in (HEA+Ni)-S1 and (HEA+Ni)-S2.

Fig. 3g, h and i depict EBSD results. According to Fig. 3h, there is no preferential orientations of grains. Moreover, no specific disorientation is observed at the chemical gradients (whose localization can be identified by comparing Fig. 3g and h). This is in line with the initial objective of having no crystal incoherency at the gradients. This should be confirmed by a characterization at a smaller scale. In sintered samples, grains are areas inside which the crystallographic orientation is constant, and which are delimited by grain boundaries (along which a crystallographic disorientation of at least 10° takes place). In Fig. 3i, the grains and the Σ3 boundaries can be observed. The grain size distribution appears homogenous and similar in the two phases. The average grain size is calculated to be 8 ± 4 µm and 9 ± 4 µm for both the HEA and the Ni phases in respectively (HEA+Ni)-S1 and (HEA+Ni)-S2 (Table 1). A grain size of 5 ± 4 µm was measured for HEA-S1 and HEA-S2, which is slightly smaller than in the architectured samples. Here again, taking into consideration the standard deviation, increasing the heating duration from 5 to 15 minutes has not enhanced the grain growth.

Finally, the sintered samples were characterized by XRD. The HEA-S1, HEA-S2 and Ni-S2 samples exhibit patterns which are similar to the ones of the powder HEA-P (results not shown here) and the lattice parameter has not evolved (Table 1). On the XRD patterns of (HEA+Ni)-P, the peaks of the Ni and HEA phases are separated while peaks overlap for (HEA+Ni)-S1 and (HEA+Ni)-S2 (Fig. 5a and Fig. S3). To appropriately fit those XRD patterns, it was necessary to add a third fcc diffracting phase, which is attributed to the interphase. According to this fit, the lattice parameter of the Ni phase was determined to be 0,35402 (2) and 0,35430 (2) nm in (HEA+Ni)-S1 and (HEA+Ni)-S2 respectively while the lattice parameter of the HEA phase was determined as 0,35900 (2) and 0,35879 (2) nm (Table 1). Thus, compared to (HEA+Ni)-P, there is a decrease of the HEA lattice parameter and an increase of the one of Ni, which is slightly more significant with the S2 sintering conditions. This can be attributed to the diffusion of Mn from the HEA phase toward the Ni phase during sintering, which was observed by SEM-EDS (Fig. 4). The lattice parameter of the interphase was determined as 0,35632 (2) and 0,35592 (2) nm in (HEA+Ni)-S1 and (HEA+Ni)-S2 respectively. This can be considered as an average parameter of this area with a varying composition.

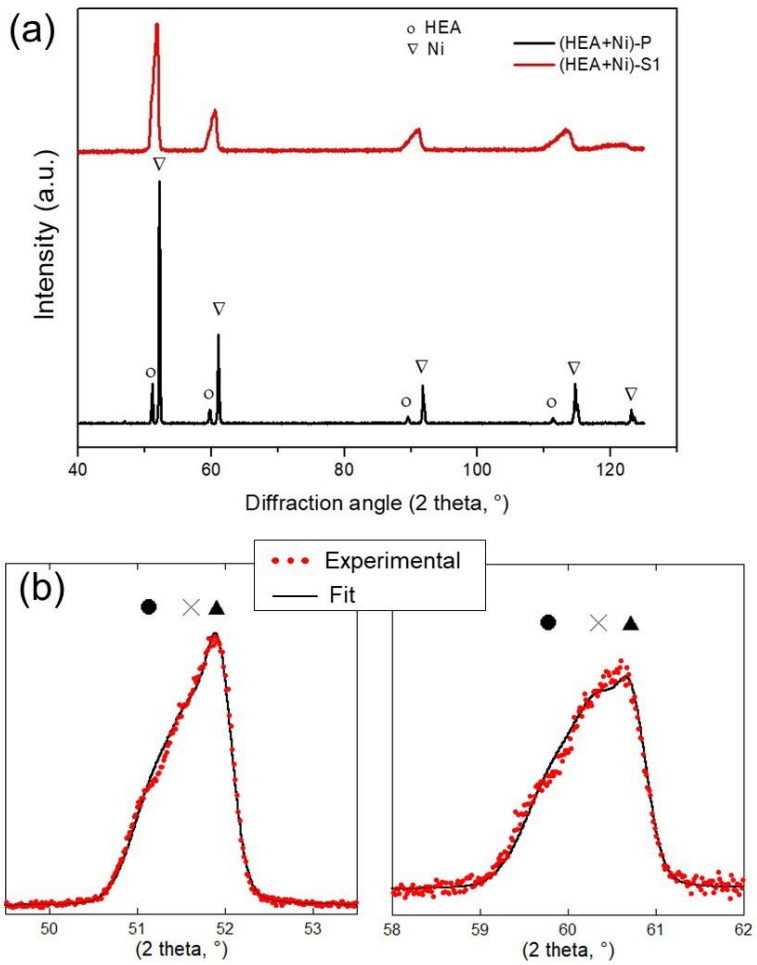

Fig. 5 : X-ray diffraction patterns of (a) (HEA+Ni)-P and (HEA+Ni)-S1, (b) zoom on the two main diffraction peaks of (HEA+Ni)-S1. Circles, crosses and triangles indicate the diffraction peaks of the HEA phase, the interphase and the Ni phase respectively, as determined by fitting.

3.3. Macroscopic and local mechanical properties

The architectured alloys (HEA+Ni)-S1 and S2, the reference samples HEA-S1, HEA-S2 and Ni-S2 were mechanically tested by compression. First, it can be seen that the engineering stress-strain curves of HEA-S1 and HEA-S2 on the one hand and of (HEA+Ni)-S1 and (HEA-Ni)-S2 on the other hand are very similar (Fig. 6). This is in agreement with the microstructural characterization (section 3.2) which has not underlined any difference between the samples processed by conditions 1 or 2. Second, the yield strengths are given in Table 1. The yield strengths of HEA-S1 and HEA-S2 are respectively 370 and 381 MPa. Otto *et al.* [35] and Sun *et al.* [36] have processed CoCrFeMnNi HEA alloys (i.e.: the same composition than HEA-S1 and HEA-S2) with varying grain sizes by melting, casting and thermomechanical treatments. For a grain size of 5 µm, a tensile yield strength of 346 and 413 MPa is calculated with the Hall & Petch coefficients of respectively Otto *et al.* [35] and Sun *et al.* [36]. Despite the fact that here compression tests were performed on HEA prepared by powder metallurgy, this is in very good agreement with our results. The yield strengths of (HEA+Ni)-S1 and (HEA+Ni)-S2 are respectively 331 and 315 MPa. Finally, the yield strength of Ni-S2 is 120 MPa. Here again, this is in very good agreement with previous measurements on bulk pure Ni with a similar grain size [37, 38]. Thus, the chemically architectured alloys are slightly softer than pure HEA and

largely stronger than pure Ni. The analysis and comparison of these values are presented in more details in section 4.3. Third, the stress continuously increases with deformation, which indicates a significant strain hardening. More specifically, since the slope of all stress-strain curves are similar, it can be qualitatively concluded that the strain hardening of references HEAs and of architectured alloys is similar. Thus, the architecturation of alloys maintains the strain hardening but does not increase it, at least for these microstructural parameters. Still, this is in favor of the ductility of chemically architectured alloys, which should be at least preserved compared to reference HEA.

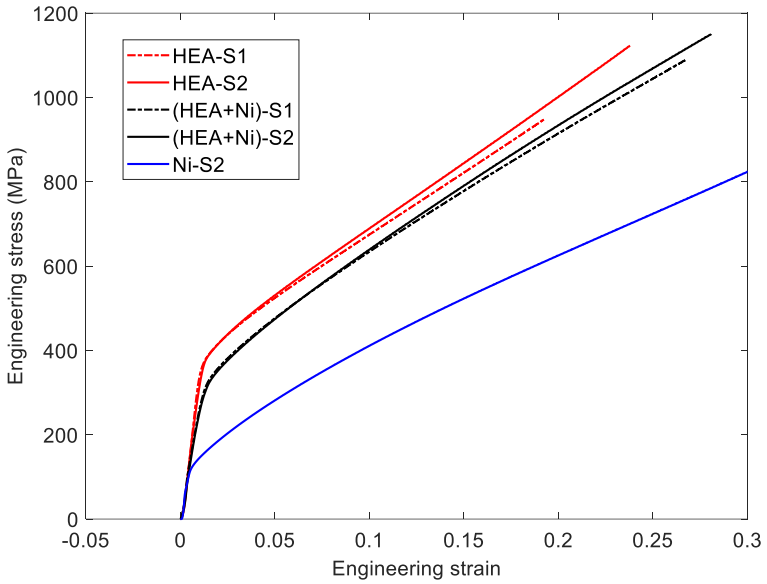

Fig. 6 : Engineering stress-strain curves of compression tests on reference single phase HEA (red curves), single phase Ni (blue curve) and on chemically architectured HEA (black curves).

Next, the hardness of each phase within chemically architectured HEA was independently measured by local nanoindentation measurements. Since the Ni and HEA phases can be optically distinguished, it was possible to precisely position the indents (Fig. 7a'). The CSM mode which was used allows to measure the hardness as a function of indentation depth. An unusual evolution of *H* indicates an interaction with a feature of the microstructure beneath the surface (i.e.: which was not optically visible), such as a change of phase. These curves were rejected (as the one indicated by a dark blue arrow on Fig. 7a). An indent depth between 350 and 400 nm was chosen as a compromise for averaging hardness (as indicated by the black arrow on Fig. 7a). It is small enough to be in the middle of an area of Ni (or HEA) phase without interactions with an area of HEA (or Ni) phase or with the interfaces. It is large enough to induce a plastic zone larger than a grain and thus to average grain boundary strengthening [39]. It is also large enough to have a limited and similar indentation size effect (ISE) for all samples. For comparison, the same conditions were applied to single phase samples (i.e.: HEA-S1, HEA-S2 and Ni-S2). The relative standard deviation on *H* is always smaller than 7 %, which confirms that the procedure is reliable and that the samples are homogeneous.

The average measured hardness for each phase within each sample are given in Table 1 and plotted in Fig. 7b. First, as expected, the hardness of HEA phases is significantly larger than the one of Ni phases in all samples (around 3.3 and 2.3 GPa respectively). Second, the hardness of both Ni and HEA phases are the same, taking into account the uncertainty, for (HEA+Ni)-S1 and (HEA+Ni)-S2. As for microstructural characterization and for compression tests, no difference is detected between the two chemically architectured HEA, sintered with different conditions. Finally, the hardness of

the Ni and HEA phases in the chemically architectured HEA and in reference samples can be compared. For the Ni phase, no difference larger than the uncertainty is observed between (HEA+Ni)-S1 and (HEA+Ni)-S2 on the one hand and Ni-S2 on the other hand. Thus, the presence of Mn within the Ni phase of chemically architectured alloys induces no significant solid solution strengthening.

For the HEA phase, the hardness is slightly larger in HEA-S1 and HEA-S2 than in (HEA+Ni)-S1 and (HEA+Ni)-S2. The diffusion of Mn during sintering has also induced a depletion of Mn in the HEA phase compared to the starting equimolar composition. This variation of composition seems to have slightly decreases the solid solution strengthening in the HEA phase. A value of the Young modulus E around 200 GPa was measured for all samples and within each phase. No influence neither of the composition nor of the processing conditions was detected for E.

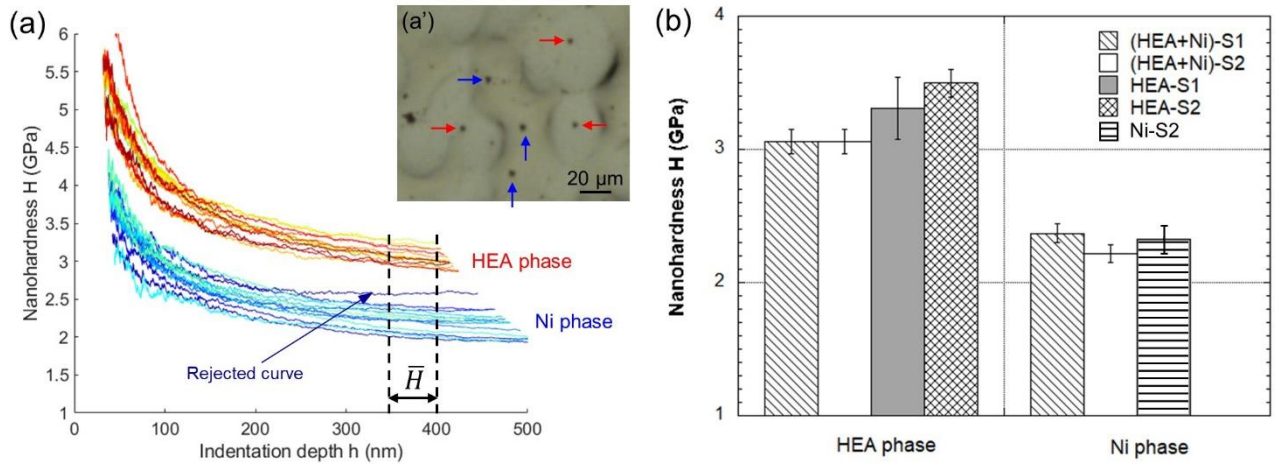

Fig. 7 : Nanoindentation measurements. (a) Evolution of nanoharndess H with indentation depth h. The curves in blue and red correspond to indents which were positioned in the Ni and HEA phases of (HEA+Ni)-S2 respectively. The range of averaging of H(h) is indicated with a black arrow. (a') Post-indentation optical image. The blue and red arrows indicate indents in the Ni and HEA phases respectively. (b) Comparison between the nanohardness of HEA and Ni phases from chemically architectured HEA and from reference samples.

4. Discussion

4.1. Influence of processing

A chemically architectured high entropy alloy has been successfully processed by spark plasma sintering (SPS). Indeed, the (HEA+Ni)-S1 and (HEA+Ni)-S2: (i) are fully densified, (ii) exhibit a homogeneous distribution of the two phases (i.e.: Ni and HEA), (iii) do not contain any unwanted phases, such as intermetallics and (iv) contain a 3D network of chemical gradients. The desired scheme of Fig. 1 is now a real material as depicted in Fig. 8. Thus, our first objective has been achieved: it is possible to process a chemically architectured alloy. Three unexpected points about the obtained chemically architectured alloys should be underlined.

First, the average width of the chemical gradients is 10 µm, which is quite large compared to the size of the HEA and Ni domains (i.e.: around 30 µm) and to the initial objective of few microns. It is underlined that these gradients were formed during a sintering duration of only 5 or 15 minutes at

the maximum temperature. Thus, the formation of the chemical gradients is very fast. It confirms that the choice of SPS technique, which allows to heat and cool very rapidly, is relevant. It also means that obtaining very thin gradients (sub-micronic for example) will be challenging.

Second, no difference of microstructural or mechanical characteristics was observed between the two chemically architectured alloys which were sintered either during 5 or 15 minutes at the maximum temperature. It means that the formation of the microstructure of chemically architectured alloys by SPS is very fast (5 minutes or less in the conditions of this study) and that, afterwards, it stabilizes. More specifically, neither the chemical gradient nor the grains grow after 5 minutes of SPS. Consequently, the plateau duration of sintering doesn't seem to be a useful parameter to tune the microstructure. Furthermore, if the microstructure stability is confirmed for longer duration, this will be an advantage for the thermal stability in use of the chemically architectured alloys.

Third, Mn spreads out nearly in the entire Ni phase. This is not the case for the other elements. This can be explained by comparing the diffusion coefficients of Co, Cr, Fe, Mn and Ni within the CoCrFeMnNi HEA, which were measured by [34, 40]. Indeed, the volume diffusion of Mn is significantly faster than the others. As a consequence of Mn diffusion, the compositions of the HEA and Ni phases in the chemically architectured alloys are different compared to the starting powders and to the reference single-phase sintered samples. It has no significant impact on the hardness of either phases. However, it decreases the difference of lattice parameter between the Ni phase and the HEA phase, which might reduce the strengthening effect of the chemical gradient. Thus, this enhanced Mn diffusion might be detrimental for the mechanical properties.

4.2. Microstructure: phases and interphase

The microstructure of chemically architectured alloys, mainly because of the presence of chemical gradients, is unprecedented. As a consequence, some terms which are usually used to describe the microstructure of metallic alloys need to be clarified. The first one is "phase". The chemically architectured alloys were described as being composed of two phases (i.e.: Ni and HEA phases). Indeed, on SEM and EDS images, two spatial domains, which are each defined by a given composition, can be observed. In opposition, the reference samples were qualified as single-phase. However, the Ni phase and the HEA phase have the same crystallographic structure (i.e.: fcc) and on a phase diagram, these two compositions belong to the same domain (i.e. : the fcc multi-component solid solution, whose composition range is very large [22]). So, from the thermodynamical point of view, Ni and HEA domains are the same phase with different composition. Now that this precision has been made for the sake of clarity, Ni and HEA domains in chemically architectured alloys will be continued to be called "phases".

Second, the chemical gradients need to be more precisely qualified. As interfaces, the chemical gradients are located at the separation between two phases (i.e.: Ni and HEA). Still, having a width of around 10 µm, they are clearly 3D and not 2D and they represent a significant volume fraction, as a phase. Moreover it seems that they do not induce any crystallographic incoherency and that they are crystalline, very likely fcc. However, the composition of chemical gradients intrinsically

varies. To illustrate their hybrid nature, we propose to name the network of chemical gradients “interphase”.

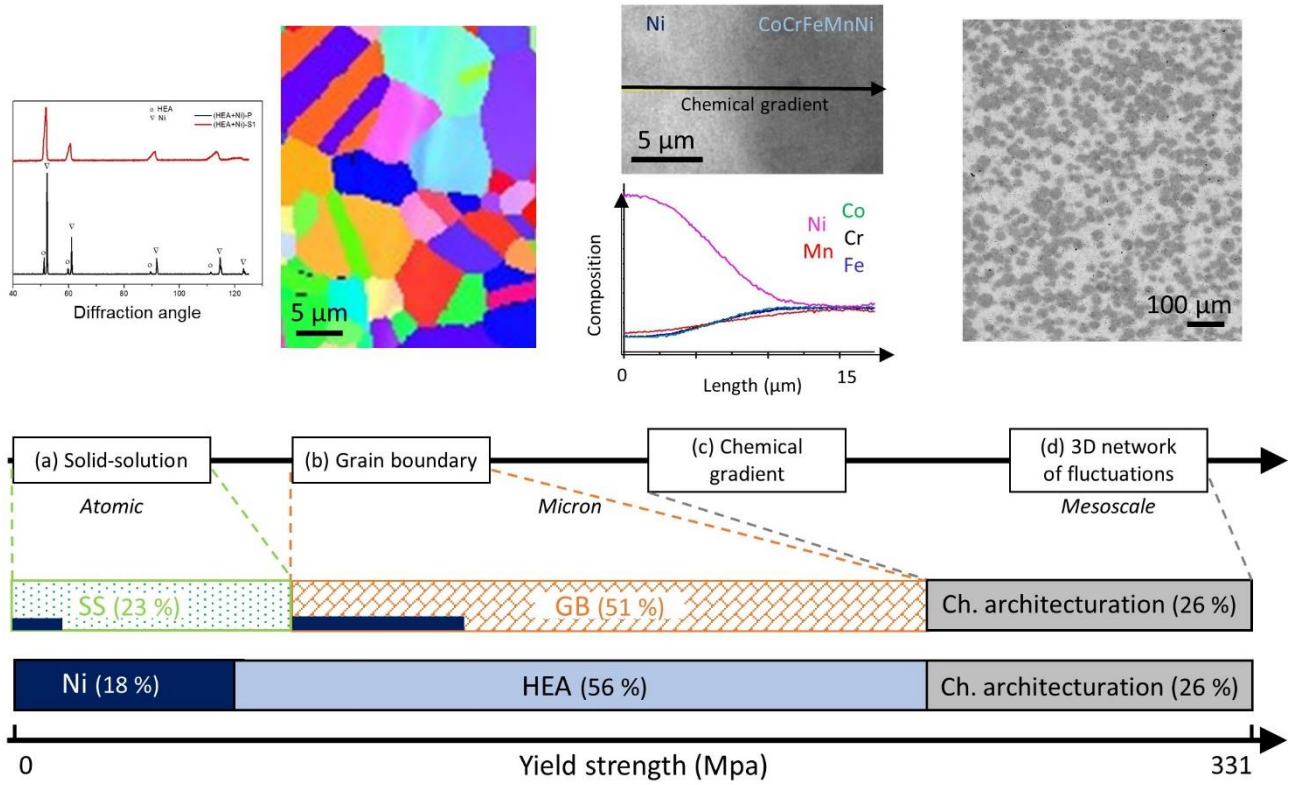

Fig. 8 : Summary of the proof of concept of chemically architectured alloys. The top line shows the characterization of the processed chemically architectured alloys at different length scale. (a), (b), (c) and (d) are XRD, EBSD, EDS profile and SEM characterizations respectively. The first line indicates the strenghening contributions of the solid solution (which also includes the Peierls stress), of the grain boundaries and of the chemical architecturation. The small dark blue rectangle represents the part of the contribution due to the Ni phase. The second line indicates the strengthening of each phase (HEA or Ni). The arrow indicates the absolute scale of yield strength.

4.3. Contributions to strengthening

The multi-scale organization of the chemically architectured alloys induces a multi-mechanism strengthening. To sort out the effect of each mechanism, reference samples, which are single-phase materials containing either the Ni phase or the CoCrFeMnNi HEA phase, were also studied. The HEA reference samples (i.e.: HEA-S1 and HEA-S2) were processed with the same conditions than the chemically architectured alloys. A similar porosity and average grain size were obtained. It is very likely that features which are induced by SPS but are difficult to quantify (such as residual stress or oxide formation) are also similar in reference HEA and architectured alloys. For the Ni reference sample, different sintering conditions were required to obtain a similar porosity. Still the previous assumption can reasonably be applied to Ni-S2. It is underlined that, due to the unexpected Mn diffusion, the compositions of the reference samples and of the two phases within chemically architectured alloys are actually slightly different. However, nanoindentation measurements have shown that this variation of composition has no effect on hardness for the Ni phase and only a slight

one for the HEA phase. Thus, the comparison of reference samples and chemically architectured alloys remains valid.

The first approach to analyze the strengthening of chemically architectured alloys is to apply a rule of mixture, as in composite materials [41]. In this rule, the contribution of each phase is considered to depend only on the volume fraction of the phase and of its strength as a single-phase material. Although this is appropriate for some materials [42, 43], there is sometimes a mechanical contrast between the phases which might induce strain incompatibilities during deformation and thus which would increase the strength. Actually, Ankem *et al.* [44] propose to systematically add an interaction term to the rule of mixture for stress-strain related properties. So here we propose to describe the yield strength of chemically architectured alloys by four terms: one for each phase (i.e.: HEA, Ni and the interphase) and the last one to take into account possible mechanical interactions between phases. It can be written as:

$$\sigma_{y,(HEA+Ni)-S} = f_{HEA} \cdot \sigma_{y,HEA} + f_{Ni} \cdot \sigma_{y,Ni} + f_{interphase} \cdot \sigma_{y,interphase} + \alpha \quad (1)$$

Where $\sigma_{y,i}$ and f_i are the yield strength and the volume fraction of the phase i and where α is the interaction term. Both the values of α and of $\sigma_{y,interphase}$ are unknown. Thus, it was preferred to group them into a single term, called σ_{chem}, which stands for the global effect of the chemical architecturation. This equation can therefore also be written as:

$$\sigma_{y,(HEA+Ni)-S} = f_{HEA} \cdot \sigma_{y,HEA} + f_{Ni} \cdot \sigma_{y,Ni} + \sigma_{chem} \quad (2)$$

$$\text{With } \sigma_{chem} = f_{interphase} \cdot \sigma_{y,interphase} + \alpha$$

σ_{chem} stands for the global effect of the chemical architecturation. Its first term is specific to this type of microstructure whereas the interaction term can be observed in other two-phase alloys. Some of the features that were proposed to contribute to this interaction, like a difference of elastic constants or specific orientation between slip systems of each phase [44], are not relevant in chemically architectured alloys of this study. So it can be expected that the contribution of the chemical gradients is major. Still, to sort out these two effects, chemically architectured alloys with varying chemical gradients will have to be compared.

Now we use Eq (2) to calculate the contribution of chemical architecturation σ_{chem}. The volume fraction can be approximated by the mass fraction given the similar lattice parameter and molar mass of Ni and HEA. Then, by using the yield strength of Ni-S2 and HEA-S1 a contribution of the Ni and HEA phases of 60 and 185 MPa respectively are calculated according to the mixture law. The remaining of the yield strength of chemically architectured alloys represents 86 MPa and corresponds to the effect of chemical architecturation σ_{chem}. Thus, there is an increase of 35 % between the yield strength as predicted by the rule of mixture and the experimental yield strength measured for (HEA+Ni)-S2. The relative contributions can also be considered (Fig. 8). The HEA phase has the main contribution (56 %) and the effect of chemical architecturation ranges in second position (26 %).

To go further into the analysis of the strengthening mechanism, the effect of grain boundaries and of the solid solution can be distinguished in Ni and HEA phase. To do so, the Hall & Petch coefficients of Keller *et al.* [37] and of Otto *et al.* [35] were used respectively for Ni and HEA. The respective contributions are also plotted in Fig. 8. The most strengthening features are the grain boundaries (51 %), then comes the chemical architecturation (26 %) and finally the solid solution (23 %), which

also includes the effect of the Peierls stress. The contribution of the Ni phase is represented by a dark blue rectangle and is, as expected, very low. Both analyses highlight that the strengthening effect of chemical gradients is significant. Thus, our second objective is also achieved: the chemical architecturation improves the mechanical properties compared to an ideal mixture of HEA and Ni.

It has to be underlined that the yield strength of these model chemically architectured HEA do not exceed the ones of existing alloys, including the reference HEA of this study. This is because the HEA was mixed with pure Ni, which is a soft metal, in order to demonstrate the concept. The versatility of this concept should permit to choose two compositions *A* and *B* with already high mechanical properties in order to increase further their yield strength.

5. Conclusion

The chemically architectured alloys were proposed as a new concept of microstructure, with a multi-scale architecturation. It evolves from a solid-solution at the atomic scale, towards grain boundaries, composition gradients and finally a 3D network of gradients at the mesoscale. Here pure Ni and CoCrFeMnNi high entropy alloy were chosen as the two phases to form a first model chemically architectured alloys. They were experimentally studied through processing by SPS, microstructural characterization by XRD and SEM coupled with EDS and EBSD and finally mechanical characterization by nanoindentation and compression tests. The main results are the following:

- Gas atomized CoCrFeMnNi and pure Ni powders are successfully densified (> 99 %) by SPS with a maximum temperature and pressure of respectively 850°C and 100 MPa, applied during 5 or 15 minutes.
- The obtained chemically architectured alloys present a homogeneous distribution of the two phases, which remain fcc, despite a slight diffusion of Mn in the Ni phase. No undesired phases were formed during SPS.
- A chemical gradient is formed in between the HEA and Ni phases. The concentration of Co, Cr, Fe and Ni vary continuously on around 10 µm. The width of variation of Mn is slightly larger.
- The compression yield strength of chemically architectured alloys is around 330 MPa. When compared to the reference Ni and HEA through a law of mixture, an increase of 35 % of the yield strength is induced by the chemical architecturation. The chemical architecturation effect is due to both the chemical gradients and the mechanical interaction between Ni and HEA phases.
- The grain boundaries contribute to 51 % of the strengthening while the contribution of chemical architecturation is of 26 %.

To conclude, the proof of concept of composition fluctuations and chemically architectured metallic alloys was achieved: processing is possible by powder metallurgy and a mechanical strengthening is induced. In the future, chemically architectured alloys with different microstructural characteristics, especially concerning chemical gradients, will be processed and characterized.

Table 1: List of the powder and sintered samples and of the main experimental data. SPS conditions indicate the temperature and duration of the plateau as well as the applied pressure. The volume porosity, lattice parameter and grain size were measured by the Archimedean method, XRD and EBSD respectively. The composition and average gradient width were measured by SEM-EDS. The yield strength and nanoharndess were measured by compression tests and nanoindentation respectively.

Name	SPS Condition	Volume fraction of porosity (%)	Lattice parameter (nm)	Grain size (μm)	Measured composition (% at.)					Average gradient width (μm)	Yield strength (Mpa)	Nanohardness (Gpa)
					Co	Cr	Fe	Mn	Ni			
(HEA+Ni)-P	No SPS	-	HEA: 0.35938 (1) Ni: 0.35238 (1)	-	HEA: dendritic microstructure Ni: 99.996 Ni					-	-	-
HEA-S1	850°C, 5 min. 100 MPa	0.74	0.36055 (3)	5 ± 4	20	20.6	20.1	19.9	19.4	-	370	3.3 ± 0.2
HEA-S2	850°C, 15 min. 100 MPa	0.14	0.36069 (6)	5 ± 4	19.9	20.6	20	20	19.5	-	381 ± 6	3.5 ± 0.1
Ni-S2	850°C, 15 min. 200 MPa	0.70	0.35270 (5)	6 ± 4	-	-	-	-	100	-	120	2.3 +/- 0.1
(HEA+Ni)-S1	850°C, 5 min. 100MPa	0.86	HEA: 0.35900 (2) Ni: 0.35402 (2)	HEA: 8 ± 4 Ni: 8 ± 4	19.5 0.7	20.9 1.5	19.4 1.3	19.7 6.5	20.5 90	10 ± 3	331 ± 10	HEA: 3.1 ± 0.1 Ni: 2.4 ± 0.1
(HEA+Ni)-S2	850°C, 15 min. 100 MPa	0.79	HEA: 0.35879 (2) Ni: 0.35430 (2)	HEA: 9 ± 4 Ni: 9 ± 4	20 0.7	20.4 1.7	20.1 1.9	19.7 6.2	19.8 89.5	10 ± 2	315 ± 5	HEA: 3.1 ± 0.1 Ni: 2.2 ± 0.1

Acknowledgements

This work benefited from a French government grant managed by ANR in the framework of the "CAMEL" (Chemically Architectured MEtallic aLloys) JCJC project, which is coordinated by M. Laurent-Brocq.

References

[1] Y. Bréchet, Filling gaps in materials space: challenges and methods, in: C.d. France (Ed.) Chaire d'Innovation technologique Liliane Bettencourt, Paris, 2013.

[2] R.O. Ritchie, The conflicts between strength and toughness, Nat. Mater., 10 (2011) 817-822.

[3] X. Wu, F. Yuan, M. Yang, P. Jiang, C. Zhang, L. Chen, Y. Wei, E. Ma, Nanodomained Nickel Unite Nanocrystal Strength with Coarse-Grain Ductility, Scientific Reports, 5 (2015) 11728.

[4] M.F. Ashby, Deformation of plastically non-homogeneous materials, Philos. Mag., 21 (1970) 399.

[5] C.C. Tasan, M. Diehl, D. Yan, M. Bechtold, F. Roters, L. Schemmann, C. Zheng, N. Peranio, D. Ponge, M. Koyama, K. Tsuzaki, D. Raabe, An Overview of Dual-Phase Steels: Advances in Microstructure-Oriented Processing and Micromechanically Guided Design, in: D.R. Clarke (Ed.) Annual Review of Materials Research, Vol 45, 2015, pp. 391-431.

[6] O. Grassel, L. Kruger, G. Frommeyer, L.W. Meyer, High strength Fe-Mn-(Al, Si) TRIP/TWIP steels development - properties - application, International Journal of Plasticity, 16 (2000) 1391-1409.

[7] E. Ma, T. Zhu, Towards strength–ductility synergy through the design of heterogeneous nanostructures in metals, Materials Today, 20 (2017) 323-331.

[8] J.W. Cahn, Hardening by spinodal decomposition, Acta Metallurgica, 11 (1963) 1275.

[9] M. Kato, T. Mori, L.H. Schwartz, Hardening by spinodal modulated structure, Acta Metallurgica, 28 (1980) 285-290.

[10] J.A. Hanna, I. Baker, M.W. Wittmann, P.R. Munroe, A new high-strength spinodal alloy, Journal of Materials Research, 20 (2005) 791-795.

[11] O. Soriano-Vargas, E.O. Avila-Davila, V.M. Lopez-Hirata, N. Cayetano-Castro, J.L. Gonzalez-Velazquez, Effect of spinodal decomposition on the mechanical behavior of Fe–Cr alloys, Materials Science and Engineering: A, 527 (2010) 2910-2914.

[12] J.C. Zhao, M.R. Notis, Spinodal decomposition, ordering transformation, and discontinuous precipitation in a Cu-15Ni-8Sn alloy, Acta Materialia, 46 (1998) 4203-4218.

[13] F. Findik, Improvements in spinodal alloys from past to present, Materials & Design, 42 (2012) 131-146.

[14] F. Danoix, P. Auger, D. Blavette, Hardening of aged duplex stainless steels by spinodal decomposition, Microscopy and Microanalysis, 10 (2004) 349-354.

[15] O. Guillon, J. Gonzalez-Julian, B. Dargatz, T. Kessel, G. Schierning, J. Rathel, M. Herrmann, Field-Assisted Sintering Technology/Spark Plasma Sintering: Mechanisms, Materials, and Technology Developments, Advanced Engineering Materials, 16 (2014) 830-849.

[16] L. Perrière, Y. Champion, F. Bernard, Spark Plasma Sintering of Metallic Glasses, in: P. Cavaliere (Ed.) Spark Plasma Sintering of Materials: Advances in Processing and Applications, Springer, 2019.

[17] M. Yu, S. Grasso, R. McKinnon, T. Saunders, M.J. Reece, Review of flash sintering: materials, mechanisms and modelling, Adv. Appl. Ceram., 116 (2017) 24-60.

[18] J.W. Yeh, S.K. Chen, S.J. Lin, J.Y. Gan, T.S. Chin, T.T. Shun, C.H. Tsau, S.Y. Chang, Nanostructured high-entropy alloys with multiple principal elements: Novel alloy design concepts and outcomes, Advanced Engineering Materials, 6 (2004) 299-303.

[19] D.B. Miracle, O.N. Senkov, A critical review of high entropy alloys and related concepts, Acta Mater., 122 (2017) 448-511.

[20] B. Cantor, I.T.H. Chang, P. Knight, A.J.B. Vincent, Microstructural development in equiatomic multicomponent alloys, Materials Science and Engineering: A, 375–377 (2004) 213-218.

[21] M. Laurent-Brocq, A. Akhatova, L. Perrière, S. Chebini, X. Sauvage, E. Leroy, Y. Champion, Insights into the phase diagram of the CrMnFeCoNi high entropy alloy, Acta Mater., 88 (2015) 355-365.

[22] G. Bracq, M. Laurent-Brocq, L. Perrière, R. Pirès, J.-M. Joubert, I. Guillot, The fcc solid solution stability in the Co-Cr-Fe-Mn-Ni multi-component system, Acta Mater., 128 (2017) 327-336.

[23] M. Laurent-Brocq, L. Perrière, R. Pirès, Y. Champion, From high entropy alloys to diluted multi-component alloys: Range of existence of a solid-solution, Materials & Design, 103 (2016) 84-89.

[24] G. Bracq, M. Laurent-Brocq, C. Varvenne, L. Perrière, W.A. Curtin, J.M. Joubert, I. Guillot, Combining experiments and modeling to explore the solid solution strengthening of high and medium entropy alloys, Acta Mater., 177 (2019) 266-279.

[25] M. Laurent-Brocq, L. Perrière, R. Pirès, F. Prima, P. Vermaut, Y. Champion, From diluted solid solutions to high entropy alloys: On the evolution of properties with composition of multi-components alloys, Materials Science and Engineering: A, 696 (2017) 228-235.

[26] M. Laurent-Brocq, P.A. Goujon, J. Monnier, B. Villeroy, L. Perrière, R. Pirès, G. Garcin, Microstructure and mechanical properties of a CoCrFeMnNi high entropy alloy processed by milling and spark plasma sintering, J. Alloys Compd., 780 (2019) 856-865.

[27] Y. Liu, J. Wang, Q. Fang, B. Liu, Y. Wu, S. Chen, Preparation of superfine-grained high entropy alloy by spark plasma sintering gas atomized powder, Intermetallics, 68 (2016) 16-22.

[28] J. Rodríguez-Carvajal, Fullprof: a program for rietveld refinement and pattern matching analysis, in: Satellite Meeting on Powder Diffraction of the XV Congress of the IUCr, Toulouse, France, 1990, pp. 13.

[29] Standard test methods for determining average grain size, ASTM International, E112-12 (2012).

[30] M. Laurent-Brocq, E. Béjanin, Y. Champion, Influence of roughness and tilt on nanoindentation measurements: A quantitative model, Scanning, 9999 (2015) 1-11.

[31] A.C. Fischer-Cripps, Analysis of nanoindentation test data, in: Nanoindentation, Springer, New York, USA, 2011, pp. 39.

[32] A. Haglund, M. Koehler, D. Catoor, E.P. George, V. Keppens, Polycrystalline elastic moduli of a high-entropy alloy at cryogenic temperatures, Intermetallics, 58 (2015) 62-64.

[33] W.B. Pearson, A handbook of lattice spacings and structures of metals and alloys, Pergamon Press, Oxford, 1967.

[34] J. Kottke, M. Laurent-Brocq, A. Fareed, D. Gaertner, L. Perrière, Ł. Rogal, S.V. Divinski, G. Wilde, Tracer diffusion in the Ni–CoCrFeMn system: Transition from a dilute solid solution to a high entropy alloy, Scr. Mater., 159 (2019) 94-98.

[35] F. Otto, A. Dlouhý, C. Somsen, H. Bei, G. Eggeler, E.P. George, The influences of temperature and microstructure on the tensile properties of a CoCrFeMnNi high-entropy alloy, Acta Mater., 61 (2013) 5743-5755.

[36] S.J. Sun, Y.Z. Tian, H.R. Lin, X.G. Dong, Y.H. Wang, Z.J. Zhang, Z.F. Zhang, Enhanced strength and ductility of bulk CoCrFeMnNi high entropy alloy having fully recrystallized ultrafine-grained structure, Materials & Design, 133 (2017) 122-127.

[37] C. Keller, E. Hug, Hall–Petch behaviour of Ni polycrystals with a few grains per thickness, Mater. Lett., 62 (2008) 1718-1720.

[38] A.W. Thompson, Effect of grain size on work hardening in nickel, Acta Metallurgica, 25 (1977) 83-86.

[39] B. Yang, H. Vehoff, Dependence of nanohardness upon indentation size and grain size – A local examination of the interaction between dislocations and grain boundaries, Acta Mater., 55 (2007) 849-856.

[40] M. Vaidya, K.G. Pradeep, B.S. Murty, G. Wilde, S.V. Divinski, Bulk tracer diffusion in CoCrFeNi and CoCrFeMnNi high entropy alloys, Acta Mater., 146 (2018) 211-224.

[41] S. Suresh, A. Mortensen, Functionally graded metals and metal-ceramic composites: Part 2 Thermomechanical behaviour, Int. Mater. Rev., 42 (1997) 85-116.

[42] Y. Wu, B. Feng, Y. Xin, R. Hong, H. Yu, Q. Liu, Microstructure and mechanical behavior of a Mg AZ31/Al 7050 laminate composite fabricated by extrusion, Materials Science and Engineering: A, 640 (2015) 454-459.

[43] Y. Wu, W.L. Song, Z.Y. Zhang, X.D. Hui, D. Ma, X.L. Wang, X.C. Shang, Z.P. Lu, Relationship between composite structures and compressive properties in CuZr-based bulk metallic glass system, Chin. Sci. Bull., 56 (2011) 3960-3964.

[44] S. Ankem, H. Margolin, A RATIONALIZATION OF STRESS-STRAIN BEHAVIOR OF 2-DUCTILE PHASE ALLOYS, Metallurgical Transactions a-Physical Metallurgy and Materials Science, 17 (1986) 2209-2226.